Journal of Materials Chemistry A

ROYAL SOCIETY OF CHEMISTRY

PAPER

View Article Online
View Journal | View Issue

Cite this: J. Mater. Chem. A, 2022, 10, 23874

Local structural distortions and reduced thermal conductivity in Ge-substituted chalcopyrite†

Sahil Tippireddy, [a] Feridoon Azough,[b] Vikram,‡[a] Animesh Bhui,[c] Philip Chater, [d] Demie Kepaptsoglou, [ef] Quentin Ramasse,[eg] Robert Freer, [b] Ricardo Grau-Crespo, [a] Kanishka Biswas, [c] Paz Vaqueiro [a] and Anthony V. Powell *[a]

Chalcopyrite, $CuFeS_2$ is considered one of the promising n-type thermoelectric materials with high natural abundance as a mineral. In this work, partial substitution of germanium in materials $CuFe_{1-x}Ge_xS_2$, ($0.0 \leq x \leq 0.10$), leads to an almost six-fold enhancement of thermoelectric properties. X-Ray photoelectron spectroscopy (XPS) reveals that germanium is present in two oxidation states: Ge^{2+} and Ge^{4+}. The stereochemically-active $4s^2$ lone-pair of electrons associated with Ge^{2+} induces a local structural distortion. Pair-distribution function (PDF) analysis reveal that Ge^{2+} ions are displaced from the centre of the GeS_4 tetrahedron towards a triangular face, leading to pseudo-trigonal pyramidal coordination. This distortion is accompanied by lattice softening and an increase of the strain-fluctuation scattering parameter (Γ_S), leading to a decrease in thermal conductivity. Phonon calculations demonstrate that germanium substitution leads to the appearance of resonant phonon modes. These modes lie close in energy to the acoustic and low-energy optical modes of the host matrix, with which they can interact, providing an additional mechanism for reducing the thermal conductivity. The weak chemical bonding of germanium with sulphur also leads to localized electronic states near the Fermi level which results in a high density-of-states effective mass, enabling a relatively high Seebeck coefficient to be maintained, despite the reduced electrical resistivity. This combination produces an almost three-fold improvement in the power factor, which when coupled with the substantial reduction in thermal conductivity, leads to a maximum figure-of-merit, $zT \sim 0.4$ at 723 K for $CuFe_{0.94}Ge_{0.06}S_2$.

Received 15th August 2022
Accepted 26th October 2022

DOI: 10.1039/d2ta06443j

rsc.li/materials-a

1. Introduction

The opportunities afforded by thermoelectric (TE) devices to harvest electrical energy from otherwise waste heat have motivated a significant worldwide search for new high-performance materials. The performance of a TE material is characterized by a figure-of-merit, $zT = S^2T/\rho\kappa$, where S, ρ and κ denote the Seebeck coefficient, electrical resistivity and thermal conductivity, respectively. While significant research effort has resulted in materials with figures-of-merit that exceed unity, many of the examples exhibiting the highest performance[1–6] contain toxic or comparatively scarce and expensive elements. Efforts to discover materials containing Earth-abundant elements have extended to an investigation of complex metal-sulphides as candidate thermoelectrics.[7,8] This has resulted in significant advances in the performance of p-type sulphides,[9–17] while progress in the n-type counterparts[18–23] required for device construction has been less marked.

Chalcopyrite, $CuFeS_2$, containing Earth-abundant elements is a candidate n-type material for thermoelectric applications. It adopts a tetragonal structure[24] (space group: $I\bar{4}2d$), which may be considered an ordered derivative of the cubic zinc blende structure, comprising vertex-sharing MS_4 (M = Cu, Fe) tetrahedra (Fig. 1). $CuFeS_2$ exhibits a moderate power factor but has a high lattice thermal conductivity that limits its thermoelectric performance. A wide range of substitutional chemistry of $CuFeS_2$ has been explored[20,25–27] in an effort to improve the electrical transport properties and hence optimize the power factor (S^2/ρ), while simultaneously reducing the lattice contribution to the thermal conductivity. Substituents have typically consisted of transition-metal cations.[20,25–28] These substituents appear to have a limited impact on the thermal conductivity as

[a]Department of Chemistry, University of Reading, Whiteknights, Reading, RG6 6DX, UK. E-mail: a.v.powell@reading.ac.uk
[b]Department of Materials, University of Manchester, Manchester, M13 9PL, UK
[c]New Chemistry Unit, Jawaharlal Nehru Centre for Advanced Scientific Research, Jakkur, Bangalore-560064, India
[d]Diamond Light Source, Harwell Science and Innovation Campus, Didcot OX11 0DE, UK
[e]SuperSTEM Laboratory, SciTech Daresbury Campus, Daresbury WA4 4AD, UK
[f]Department of Physics, University of York, York YO10 5DD, UK
[g]School of Chemical and Process Engineering, University of Leeds, Leeds LS2 9JT, UK

† Electronic supplementary information (ESI) available. See DOI: https://doi.org/10.1039/d2ta06443j

‡ Present address: Department of Materials, University of Oxford, Parks Road, Oxford OX1 3PH, UK.

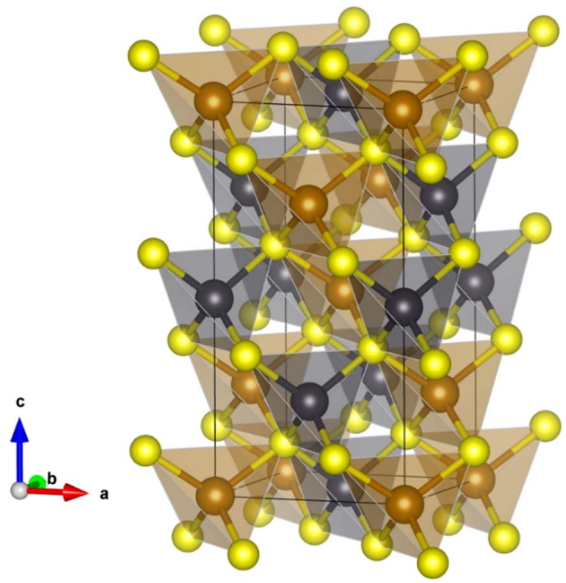

Fig. 1 Tetragonal crystal structure of $CuFeS_2$ (space group $I\bar{4}2d$) showing the vertex-sharing MS_4 (M = Cu, Fe) tetrahedra; where Cu (orange), Fe (grey) and S (yellow) atoms occupy the 4a, 4b and 8d Wyckoff sites respectively.

they do not produce any significant anharmonicity or induce substantial structural distortions.

We are engaged in a program of work to exploit substitution with high oxidation state main-group cations, to enhance the TE performance of chalcopyrite. The different bonding properties of such substituents compared to transition-metal cations, may lead to weaker chemical bonding and potentially introduce structural distortions. Such features can have a marked impact on the phonon density of states and contribute to reductions in the lattice thermal conductivity.[29,30] High oxidation state substituents offer the potential to achieve greater increases in the charge-carrier concentration than is possible with the more usual 2+ transition-metal cations. Although, as we have demonstrated recently,[31] in the case of substitution with Sn^{4+}, the increase in charge-carrier concentration can deviate from expected values due to the presence of localised states, associated with the formation of small polarons.

Here we describe the impact on electrical and thermal transport properties of substitution of Fe^{3+} by the p-block element, Ge^{4+}, in chalcopyrite. X-Ray photoelectron spectroscopy (XPS) reveals the presence of germanium in two oxidation states, Ge^{4+} and Ge^{2+}, in the substituted phases. While the charge-carrier concentration is increased on substitution, the formation of Ge^{2+} limits the increase to values below that expected on the basis of formal electron-counting. Significantly, the different bonding preferences of Ge^{2+} arising from the non-bonding $4s^2$ electron pair, induce a local structural distortion, in which the Ge^{2+} cation is displaced from the centre of a GeS_4 tetrahedron towards one of the triangular faces of the polyhedron. This induces lattice softening and enhances phonon scattering, resulting in a lattice thermal conductivity that is less than half of that in the pristine phase. Although substitution decreases the electrical resistivity, a relatively high Seebeck coefficient is maintained, leading to an increase in power factor. This, together with a marked reduction in thermal conductivity, leads to an almost six-fold increase in the figure-of-merit.

2. Methods

Elemental Cu (Sigma Aldrich, 99.5%), Fe (Alfa Aesar, 99%+), Ge (Fisher Scientific, 99.999%) powders and S flakes (Sigma Aldrich, 99.99%) were weighed in stoichiometric amounts according to the formula, $CuFe_{1-x}Ge_xS_2$ ($0 \leq x \leq 0.1$) and sealed into evacuated ($\sim 10^{-3}$ mbar) fused silica tubes. The evacuated tubes were heated to 723 K and held at this temperature for 150 hours before slow cooling (0.4 K min^{-1}) to room temperature. The products were ground and re-fired for 48 hours at 1173 K in evacuated silica tubes, before cooling to room temperature at 0.4 K min^{-1}. The as-cast ingots were re-ground and hot-pressed at 873 K under a pressure of 80 MPa for 30 minutes. Densities of the consolidated pellets, determined by the Archimedes method, using an AE Adam PW 184 balance, are >98% of the theoretical value.

Initial phase analysis of the powdered products was carried out by laboratory powder X-ray diffraction, collected using a Bruker D8 Advance diffractometer (Cu $K_{\alpha 1}$: $\lambda = 1.5405$ Å). Synchrotron X-ray powder diffraction data ($\lambda = 0.161669$ Å) were collected on the I15-1 beamline at the Diamond Light Source synchrotron facility, UK. The PerkinElmer XRD 1611 CP3 Bragg detector was placed ~900 mm from the sample for a data acquisition time of 120 s. Rietveld analysis of the powder X-ray diffraction data was carried out using FullProf.[32] X-Ray total scattering data for $CuFe_{1-x}Ge_xS_2$ ($0.02 \leq x \leq 0.1$) were collected on I15-1 using a PerkinElmer XRD 4343 CT detector placed ~200 mm from the sample, with a data acquisition time of 300 s. The powder samples were contained in 1 mm capillaries, which were spun during data collection. The diffraction data were processed using the GudrunX software[33] ($Q_{max} = 30$ Å) to perform background and instrumental corrections and to convert the data into the pair-distribution function (PDF). The PDF analysis (small box modelling) and fitting was performed using the PDFgui software.[34]

X-Ray photoelectron spectroscopy (XPS) measurements for $CuFe_{0.94}Ge_{0.06}S_2$ were performed with a Thermo Scientific spectrometer using an Al-Kα (1.487 keV) X-ray monochromatic source with variable spot size. The C 1s binding energy (284.8 eV) was used for calibration. The background correction, peak deconvolution and fitting of the XPS spectra were carried out using CasaXPS software.[35]

The microstructure was investigated using a SIRION FEI FEG-SEM, and energy-dispersive X-ray spectroscopy (EDS) elemental point analysis was performed using a TESCAN MIRA LC FEG (SEM) equipped with an Oxford Instrument SDD energy dispersive detector. An FEI FEGTEM (Tecnai G2, Hillsboro, OR) operating at 300 kV was used for high-resolution transmission electron microscopy (HRTEM) and selected area electron diffraction (SAED). Atomic-resolution structural characterization was carried out using a Nion UltraSTEM aberration-

corrected STEM equipped with a Gatan Enfina electron energy loss spectrometer. This microscope was operated at 100 kV acceleration voltage and the probe-forming optics were adjusted to form a 0.9 Å electron probe with a convergence of 31 mrad and beam current of approximately 50 pA.

Electrical resistivity and Seebeck coefficient data were collected on hot-pressed pellets over the temperature range ($323 \leq T/K \leq 723$) using a Linseis LSR-3 system. Hall effect measurements at room temperature were performed using an Ecopia HMS-3000 system. Thermal diffusivity (α), data were collected using a Netzsch LFA-447 NanoFlash instrument ($323 \leq T/K \leq 573$) and an Anter Flashline-3000 system ($573 \leq T/K \leq 723$ K). The data were converted to thermal conductivity (κ) using $\kappa = \alpha C_p d$ where C_p denotes the constant-pressure specific heat capacity, and d is the sample density. The specific heat of chalcopyrite was calculated to be 0.52 J g^{-1} K^{-1}, using the Dulong–Petit expression. Uncertainties in electrical resistivity, Seebeck coefficient and thermal conductivity are estimated to be 5%, 5% and 10% respectively, leading to an estimated uncertainty in the figure-of-merit (zT) of *ca.* 15%. Longitudinal (v_l) and transverse (v_t) sound velocity measurements were performed at room temperature, on an ingot of dimensions: 12.7 mm (diameter) × 1.8 mm (thickness), using an Olympus Epoch 650 Ultrasonic Flaw Detector with a transducer frequency of 5 MHz.

Density functional theory (DFT) calculations were performed using the VASP code[36–38] and a projected augmented-wave basis with a wave cutoff of 385 eV.[39] The generalized gradient approximation (GGA) exchange–correlation functional of Perdew–Burke–Ernzerhof (PBE)[40] was used, and a Hubbard (GGA + U) correction with $U_{eff} = 3$ eV was applied to improve the poor GGA description of the Fe 3d orbitals.[41] To simulate the 6 at% Ge substituted $CuFeS_2$ approximating the experimental composition, $CuFe_{0.94}Ge_{0.06}S_2$, a supercell of 2 × 2 × 1 conventional unit cell of $CuFeS_2$ (with $Z = 4$ in each conventional unit cell) was taken where one atom of Fe was replaced by Ge. This gives a composition with 6.25 at% Ge substituted in $CuFeS_2$, or $CuFe_{0.9375}Ge_{0.0625}S_2$, close to the experimental composition. The zero-damping DFT-D3 method[42] was employed and the structure was relaxed with a threshold force of 10^{-4} eV $Å^{-1}$ on each atom. The resulting lattice parameters are in close agreement with the experimental values. The Brillouin zone was sampled by a 4 × 4 × 2 and 12 × 12 × 6 Γ-centered k-point mesh for structural optimization and single

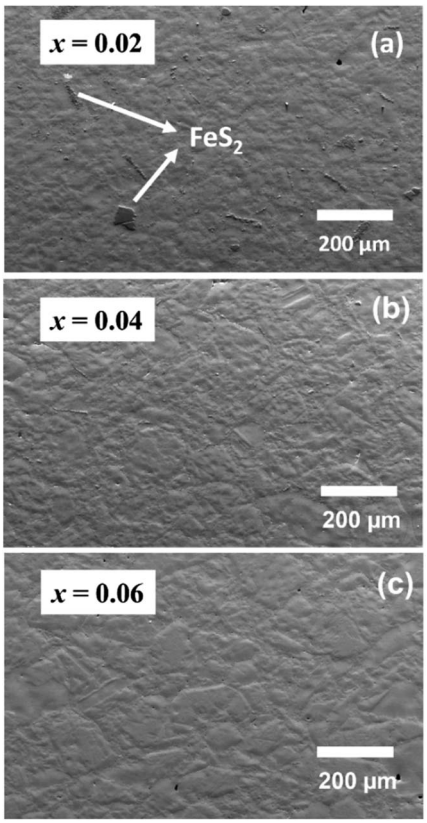

Fig. 3 Scanning electron microscopy (SEM) images for $CuFe_{1-x}Ge_xS_2$ with (a) $x = 0.02$, (b) $x = 0.04$ and (c) $x = 0.06$.

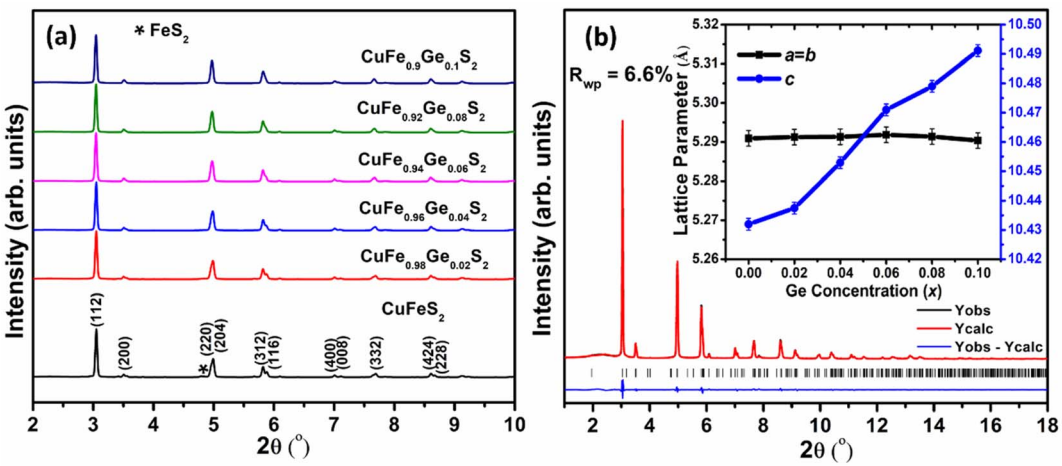

Fig. 2 (a) Synchrotron X-ray powder diffraction patterns ($\lambda = 0.161669$ Å) collected for $CuFe_{1-x}Ge_xS_2$ ($0.0 \leq x \leq 0.10$). (b) Rietveld refinement using powder X-ray diffraction data for $CuFe_{0.94}Ge_{0.06}S_2$. The inset shows the lattice parameters as a function of Ge content (x).

point calculations respectively, with reference to the conventional unit cell and using grids of the same density for supercell calculations. Spin-polarization was allowed in the simulations, and the Fe magnetic moments were initialized in high-spin configurations with antiferromagnetic ordering. The electronic density of states (DOS) was calculated using the tetrahedron method with Blöchl corrections.[43] The phonon dispersion curves for the 6.25% Ge doped composition were obtained using density functional perturbation theory (DFPT)[44,45] as implemented in VASP, to first calculate the force constants, and later using the PHONOPY[46] code, for force constant extraction and calculation of the dispersion plot.

3. Results and discussion

Examination of laboratory powder X-ray diffraction data indicated that all compositions could be indexed on the basis of a tetragonal unit cell, with lattice parameters similar to those of $CuFeS_2$, thereby confirming that the chalcopyrite structure is retained at all levels of substitution. Subsequent structural analysis was conducted using powder X-ray diffraction data obtained using synchrotron radiation (Fig. 2a). The powder diffraction data for the Ge-substituted materials provide no evidence for the presence of any impurity phases, while a weak feature arising from trace amounts of FeS_2 is apparent in the data for the end-member, $CuFeS_2$. Rietveld refinements using synchrotron X-ray powder diffraction data (Fig. 2b for $CuFe_{0.94}Ge_{0.06}S_2$, with data for the remaining compositions provided as ESI†) were carried out using a structural model in which Ge is located at the Fe (4b) site. This results in excellent agreement between the observed and calculated powder diffraction patterns. While the unit-cell parameter, a, remains almost constant (Fig. 2b (inset)) with increasing Ge content, the c parameter increases monotonically. Since the ionic radii of Ge^{4+} and Fe^{3+} in tetrahedral coordination are 0.39 and 0.49 Å respectively,[47] Ge^{4+} substitution at the Fe^{3+} site would be expected to result in a slight decrease in the lattice parameters. However, as demonstrated by XPS data (*vide infra*), Ge-substituted materials also contain larger Fe^{2+} (0.63 Å) and Ge^{2+} (0.73 Å) cations,[47] which may be responsible for the observed increase in the c lattice parameter.

Scanning electron microscopy (SEM) coupled with energy-dispersive X-ray spectroscopy (EDS) was performed to evaluate the composition of the samples and to identify any trace amounts of secondary phases, below the level of detection by powder X-ray diffraction, that may influence the transport properties. The SEM data (Fig. S2a†) for $CuFeS_2$ itself, indicate the presence of small amounts of FeS_2 and Cu_5FeS_4. Similarly, at the lowest level of Ge substitution ($x = 0.02$), trace amounts of FeS_2 are observed (Fig. 3a), albeit reduced compared to the unsubstituted sample. At Ge contents in the range $0.04 \geq x \geq 0.06$, the SEM data (Fig. 3b and c) show the materials to be

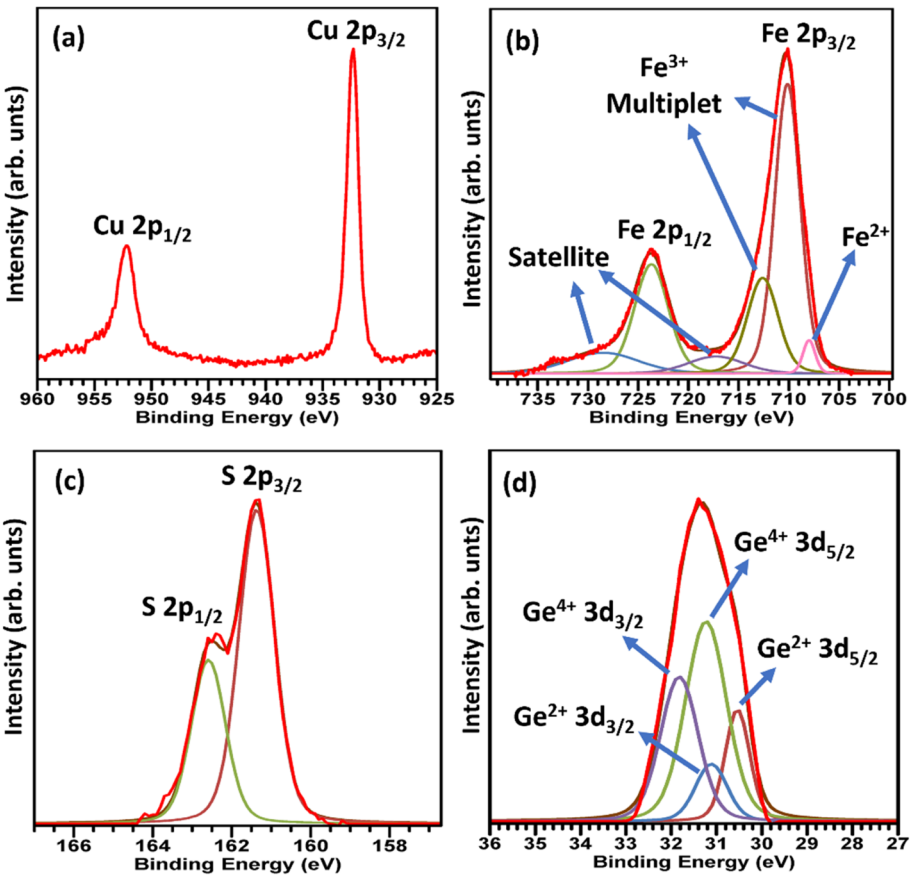

Fig. 4 The X-ray photoelectron spectra corresponding to (a) Cu 2p (b) Fe 2p (c) S 2p (d) Ge 3d in $CuFe_{0.94}Ge_{0.06}S_2$.

phase-pure with no evidence of any secondary phase(s), suggesting that Ge substitution stabilizes the chalcopyrite phase and suppresses the formation of secondary phases. At the highest levels of germanium incorporation, ($x > 0.06$), FeS_2 together with microprecipitates of another secondary phase, identified by EDS as a non-stoichiometric, copper-poor chalcopyrite-like phase (the compositions of which are presented in the caption to Fig. S2†) are evident at very high magnification (Fig. S2b and c†).

The compositions of the principal chalcopyrite-type phase in the substituted samples, determined by EDS (Table S2†), are broadly consistent with the nominal compositions. The slightly higher Cu contents determined by EDS may be due to the overlap of the K_α and L_α characteristic lines of Cu and Fe, as has been reported previously.[31] The Ge contents are in excellent agreement with the nominal values, indicating successful substitution of Ge in the chalcopyrite matrix.

X-Ray photoelectron spectroscopy data for $CuFe_{0.94}Ge_{0.06}S_2$ (Fig. 4) reveals the presence of Cu^+, Fe^{3+} and S^{2-}, as has been observed in XPS data for unsubstituted chalcopyrites.[25,29,31,48,49] However, an additional weak peak (Fig. 4b) corresponding to Fe^{2+} is observed in the Fe 2p spectrum, suggesting that Ge substitution results in a reduction of a fraction of the Fe^{3+} ions to Fe^{2+}. A similar observation has been made for tin and indium substitution in chalcopyrite[30,31] Significantly, the 3d spectrum of Ge (Fig. 4d) indicates that this cation is in a mixed oxidation state, with peaks assignable to both Ge^{2+} and Ge^{4+} present; the latter having the higher intensity. While data were obtained for materials with lower germanium contents, the Ge signal was too weak to provide definitive information on the oxidation states.

$CuFeS_2$ exhibits a relatively high electrical resistivity (ρ) of 0.31–0.4 mΩ m at temperatures in the range $323 \leq T/K \leq 723$. The resistivity is markedly reduced on Ge substitution (Fig. 5a) at levels of substitution up to $x = 0.06$. The temperature dependence also changes, with $\rho(T)$ becoming relatively flat for the substituted materials. At higher levels of Ge incorporation, ($x \geq 0.08$) the electrical resistivity increases slightly. This may be associated with the presence of trace amounts of secondary phases, identified by SEM, at these high levels of substitution. The lowest electrical resistivity, measured for $CuFe_{0.94}Ge_{0.06}S_2$, is *ca.* 50–70% lower than that of the pristine $CuFeS_2$ phase, demonstrating the effectiveness of Ge substitution in improving the electrical properties.

The Seebeck coefficient (S) (Fig. 5b), follows a similar trend to that observed for the electric resistivity: $|S|$ initially decreases with Ge contents up to $x = 0.06$, before increasing slightly at $x \geq 0.08$. The temperature dependence of the Seebeck coefficient is again markedly different for the substituted samples, and $S(T)$ exhibits a much flatter response compared to that of $CuFeS_2$. A low electrical resistivity combined with a relatively high and flat $S(T)$, leads to a high power-factor (PF) in the Ge-substituted phases, which increases with temperature, contrary to the PF(T) dependence of $CuFeS_2$ (Fig. 5c). The maximum power factor, PF = 0.6 mW m^{-1} K^{-2}, achieved for $CuFe_{0.94}Ge_{0.06}S_2$ at 723 K, represents an almost three-fold improvement over that of unsubstituted $CuFeS_2$.

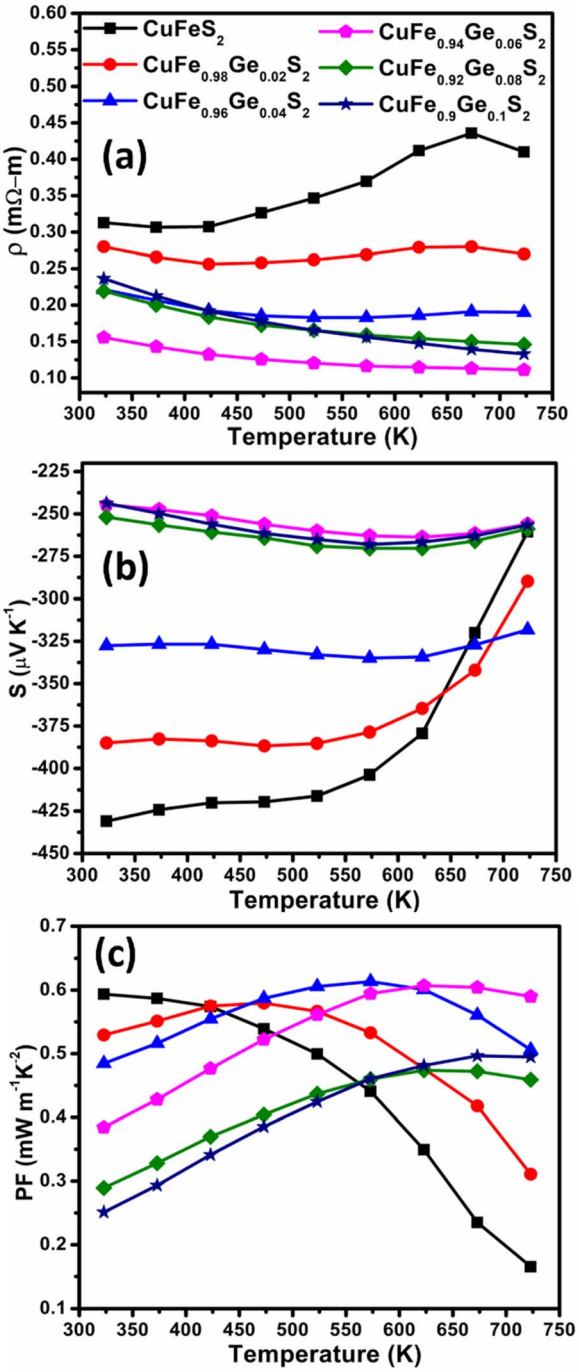

Fig. 5 (a) Electrical resistivity (ρ), (b) Seebeck coefficient (S) and (c) power factor (PF) as a function of temperature of $CuFe_{1-x}Ge_xS_2$ ($0.0 \leq x \leq 0.10$).

Hall-effect measurements at room temperature (Fig. 6a), reveal that the charge-carrier concentration (n) increases with increasing Ge concentration, from $n = 1.4(2) \times 10^{19}$ cm^{-3} for unsubstituted $CuFeS_2$ to a maximum $n = 4.7(3) \times 10^{19}$ cm^{-3} for $CuFe_{0.94}Ge_{0.06}S_2$. However, the maximum value of n is lower than that expected on formal electron counting grounds (*ca.* 8×10^{20} cm^{-3} for $x = 0.06$). While substitution of Ge^{4+} for Fe^{3+} results in electron donation, Ge^{2+} identified by XPS, is expected

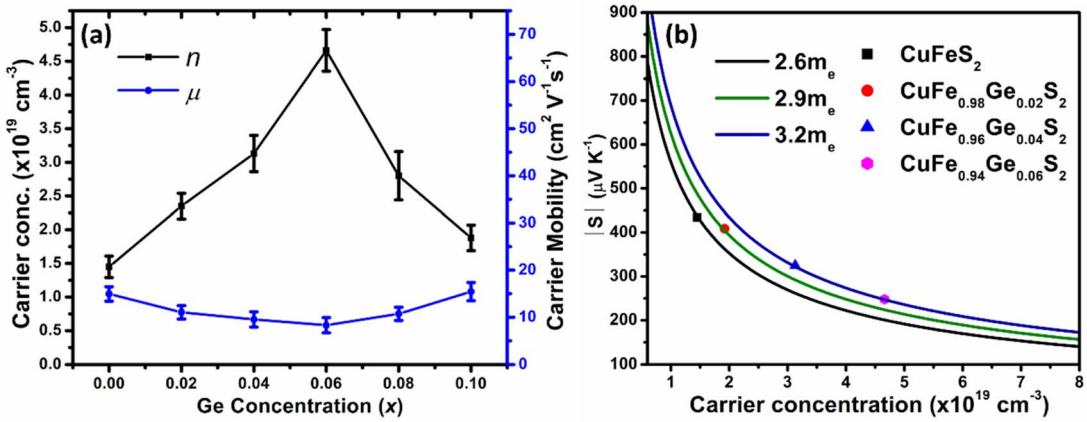

Fig. 6 (a) Carrier concentration (n) and mobility (μ) of $CuFe_{1-x}Ge_xS_2$ ($0.0 \leq x \leq 0.10$) samples. (b) Pisarenko plot showing $|S|$ *vs.* n for $CuFe_{1-x}Ge_xS_2$ ($0.0 \leq x \leq 0.06$) samples.

to act as an electron acceptor. The intensity ratio $I(Ge^{4+})/I(Ge^{2+}) \approx 2.5$ observed in the XPS data, indicates that Ge^{4+} is the majority species. Therefore, germanium substitution is expected to produce an increase in the effective carrier concentration, albeit one that is reduced from the values expected on the basis of electron counting.

With further increases in the Ge content ($x > 0.06$), the carrier concentration decreases, consistent with the slight increase in the electrical resistivity and Seebeck coefficient for the compositions with $x \geq 0.08$. The origin of the decrease in charge-carrier concentration at high levels of substitution may be associated with the formation of secondary phase(s), as observed by SEM (but not by powder X-ray diffraction), that would result in a slight change to the Cu : Fe ratio in the primary chalcopyrite-type phase. Although the charge-carrier mobility decreases with substitution, the change is less marked compared to that in the carrier concentration. Pisarenko plots (Fig. 6b) derived from the Hall measurement data reveal an increase in the density-of-states (DOS) effective mass, from $m_d^* = 2.6\ m_e$ for the $CuFeS_2$ to $m_d^* = 2.9 - 3.2\ m_e$ for $CuFe_{1-x}Ge_xS_2$ ($0.02 \leq x \leq 0.06$). The increase in m_d^* can be understood from the atom projected density of states (PDOS) for the Ge-substituted $CuFeS_2$ system (Fig. 7). Localized germanium electronic states near the Fermi level (E_F), indicate weak chemical bonding with the sulphur atoms. The hybridization of germanium 4p states with sulphur 3p states also induces localized iron and copper electronic states. These are associated with those neighbouring MS_4 (M = Fe, Cu) tetrahedra that are

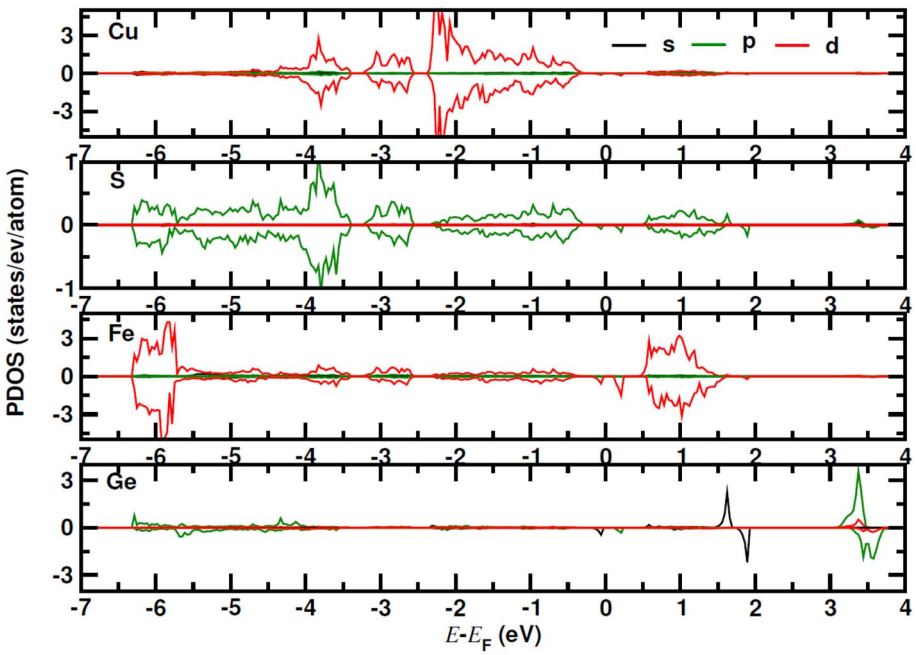

Fig. 7 The atom projected density of states (PDOS) for Ge (6.25 at%) substituted $CuFeS_2$ system.

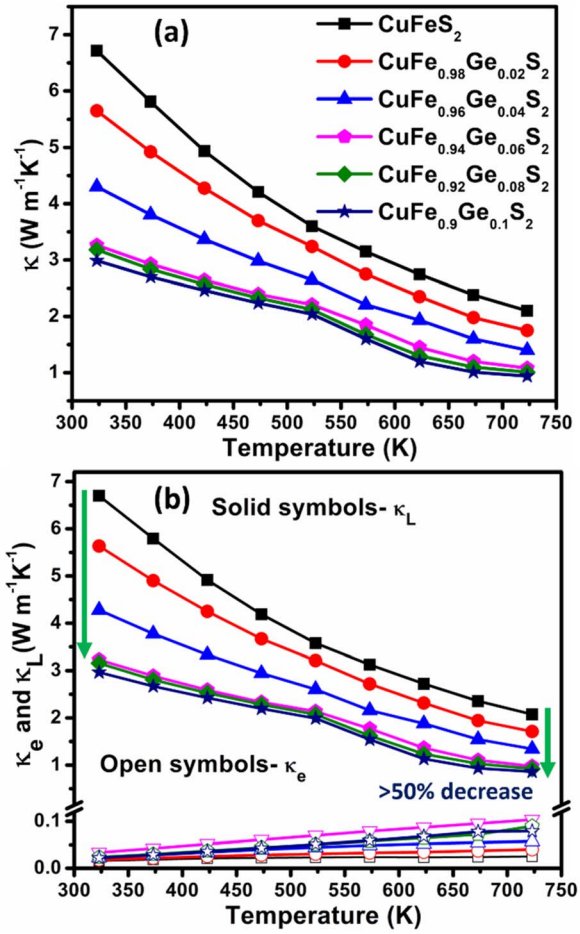

Fig. 8 Temperature dependence of (a) total (κ), (b) electronic (κ_e) and lattice (κ_L) thermal conductivities of $CuFe_{1-x}Ge_xS_2$ ($0.0 \leq x \leq 0.10$).

connected to the germanium-centered tetrahedra through a common sulphur vertex. The sharp localized states increase the band degeneracy and the DOS near the Fermi level, and are responsible for the high m_d^*, which contributes to the maintenance of a relatively high Seebeck coefficient.

Unsubstituted $CuFeS_2$ exhibits a high thermal conductivity (Fig. 8a) due to a large lattice component (κ_L) (Fig. 8b), arising from a high mean sound velocity (Table 1). The lattice component, κ_L, decreases by more than 50% on Ge substitution (for $x \geq 0.06$) with a correspondingly marked reduction in the mean sound velocities. The derived Debye temperature and elastic moduli also decrease considerably with Ge substitution, indicative of significant lattice softening.

Previously,[31] it has been shown that scattering of acoustic phonons with mean free paths between 50 and 500 nm, can reduce the lattice thermal conductivity of chalcopyrite-type phases significantly. High-resolution transmission electron microscopy (HRTEM) ($x = 0.06$ and 0.1) and TEM ($x = 0.1$) along the [110] zone axis show twinning features and dislocations in the Ge-substituted phases at length scales in the range of 5–20 nm. The density of twins/dislocations become more prominent with an increase in the Ge content (Fig. 9a and c). However, these line defects would scatter acoustic phonons with only a small range of mean free-paths. While this may contribute to the reduction in the lattice thermal conductivity, the scattering is insufficient to account for the observed substantial reduction in κ_L.

The selected area electron diffraction (SAED) pattern along the [110] zone axis for the composition $x = 0.06$ (Fig. 9b) shows no additional diffraction spots corresponding to lower-symmetry superstructures and/or other phases, apart from the tetragonal chalcopyrite structure, which is consistent with powder X-ray diffraction and SEM data. Furthermore, to investigate if the origin of the reduction in lattice thermal conductivity is associated with atomic scale defects in the substituted phases, atomic resolution scanning transmission electron microscopy (STEM) was performed for $CuFe_{0.94}Ge_{0.06}S_2$. The high-angle annular dark field (HAADF)-STEM image (Fig. 9e) at high magnification reveals no short/long range atomic disorder or vacancies and shows a uniform and homogenous atomic ordering in the substituted materials. The absence of any secondary phases and of atomic defects/vacancies, combined with the limited range of mean-free-paths of acoustic phonons scattered by twins/dislocations, suggests that microstructural features are not the primary origin of the reduced lattice thermal conductivity.

To investigate the origin of the reduction in thermal conductivity further, pair distribution function (PDF) analysis of synchrotron X-ray total scattering data was performed for $CuFe_{1-x}Ge_xS_2$ ($0.02 \leq x \leq 0.1$) to explore changes in the local bonding and coordination. The initial structural model in which Cu, Fe/Ge and S occupy the 4a, 4b, and 8d sites respectively, with site occupancy factors corresponding to the nominal stoichiometry, was obtained from Rietveld refinement using synchrotron X-ray powder diffraction data. This was imported to PDFgui to model the experimental PDF. A systematic refinement of the lattice parameters, atomic positions, thermal displacement parameters and occupancies was performed in PDFgui over the range $0 < r < 20$ Å. At this stage, the long-range average structure provided a reasonably good fit (R_w = 9.8–

Table 1 The longitudinal (v_l), transverse (v_t), average (v_{avg}) and mean (v_m) sound velocities; Young's (E) and shear (G) moduli, and Debye temperature (θ_D) of $CuFe_{1-x}Ge_xS_2$ ($0.0 \leq x \leq 0.10$). The calculation details for these parameters are provided in the ESI

Sample	v_l [m s^{-1}]	v_t [m s^{-1}]	v_{avg} [m s^{-1}]	v_m [m s^{-1}]	E [GPa]	G [GPa]	θ_D [K]
$x = 0$	4720	2536	3264	2831	69.9	26.94	319
$x = 0.02$	4178	2270	2906	2532	55.59	21.54	286
$x = 0.06$	3690	2135	2653	2370	47.46	19.00	267
$x = 0.1$	3470	2122	2571	2342	44.36	18.46	264

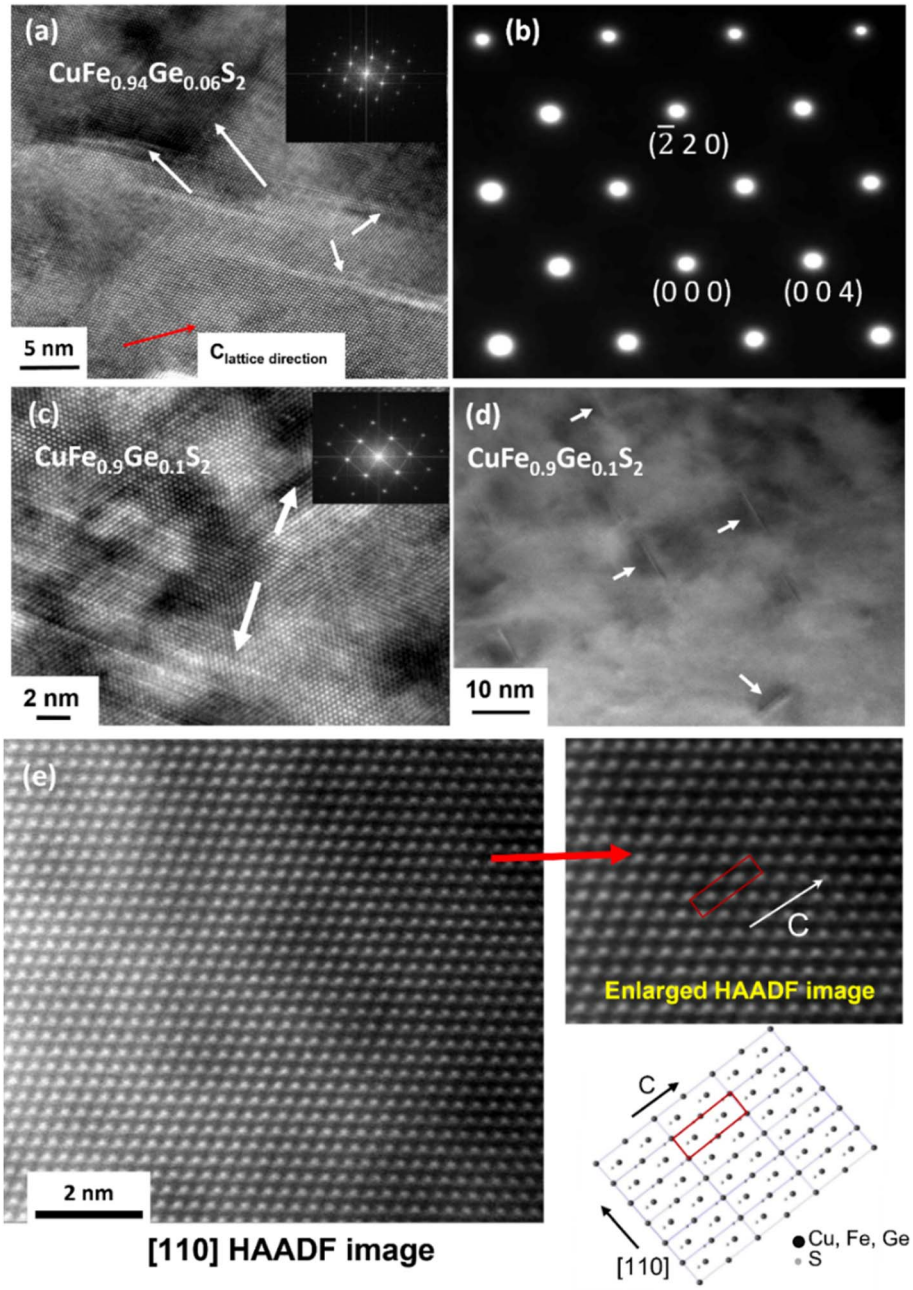

Fig. 9 (a) High-resolution transmission electron microscopy (HRTEM) image and (b) selected area electron diffraction pattern (SAED) along the [110] zone axis for $CuFe_{0.94}Ge_{0.06}S_2$. (c) HRTEM and (d) TEM images along [110] zone axis for $CuFe_{0.9}Ge_{0.1}S_2$ (e) HAADF-STEM image along the [110] axis. Enlarged colour HAADF image showing the distribution of cations is given in the ESI.†

11.2%) to the PDF at longer interatomic distances (r) but produced relatively poor agreement between the calculated and observed PDF at lower r (<3 Å), indicating the presence of short-range deviations from the long-range average structure. In an effort to improve the fit at low r, the symmetry constraints on the Wyckoff sites were relaxed and atomic positions for each cation and anion refined sequentially, unconstrained by symmetry. The coordinates for Cu, Fe and S remained unchanged, thereby maintaining the overall crystal symmetry and long-range order of these cations. However, the model that produced the best fit (R_w = 5.6–6.1%) of the PDF for all substituted phases corresponds to a structure in which two out of the four germanium positions originally at the 4b site in the unit cell are displaced from the centre of the GeS_4 tetrahedron towards one of the triangular (S_3) faces of the tetrahedron. The resulting experimental and calculated PDFs for $CuFe_{0.94}Ge_{0.06}S_2$ are presented in Fig. 10, with the profiles for the other compositions provided as ESI, (Fig. S6†). The remaining two Ge positions remain in the expected tetrahedral geometry at locations corresponding to a sub-set of those associated with what

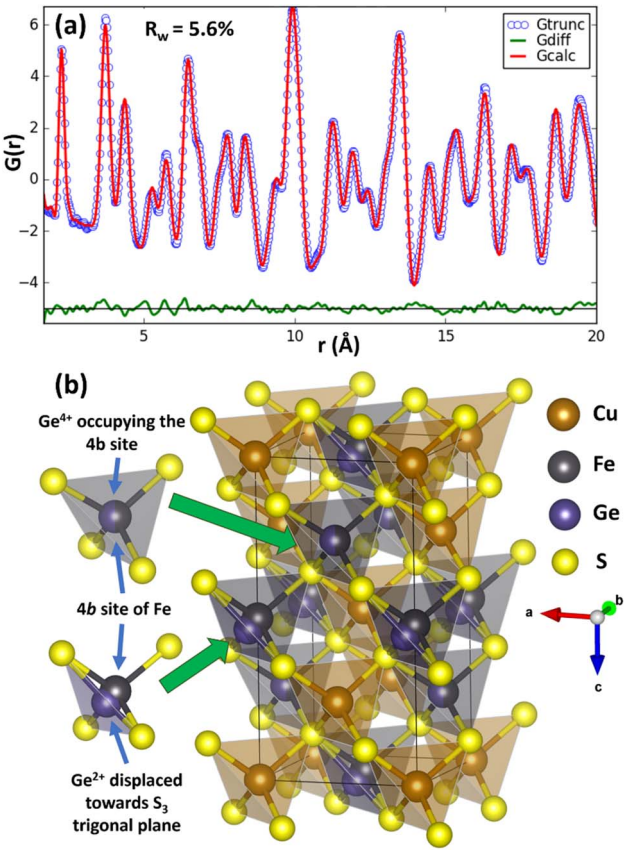

Fig. 10 (a) Pair-distribution function, $G(r)$ as a function of atomic-pair distance (r) for $CuFe_{0.94}Ge_{0.06}S_2$ (x = 0.06). G_{trunc} and G_{calc} represent the experimental and calculated PDFs respectively, while $G_{diff} = G_{trunc} - G_{calc}$. (b) The best fit structural model showing local distortion induced by Ge^{2+} ions.

was originally the single 4b Wyckoff site. The germanium cations remaining in tetrahedral coordination can be associated with the Ge^{4+} ions identified by XPS. The closed-shell $3d^{10}$ electron configuration of this cation supports a stable tetrahedral coordination by sulphur atoms. The off-centered Ge cations can be identified as the Ge^{2+} species. These exhibit a near trigonal pyramidal coordination with three sulphur atoms (Fig. 10), instead of the expected tetrahedral coordination. The splitting of these two Ge^{2+} cations out of the four formerly crystallographically equivalent sites, maximises the distance between Ge^{2+} which aids in maintaining the local charge balance. Moreover, the level of Ge substitution is too low to induce long-range order, and the average structure is therefore not affected by the local distortion. A similar mixed coordination environment of germanium with sulphur has been observed in $TlGeS_2$,[50] which contains formally Ge^{4+} in tetrahedral coordination (GeS_4) and Ge^{2+} in a distorted trigonal pyramidal coordination (GeS_3). Similarly, in germanium(II) sulfide, GeS, Ge^{2+} adopts a trigonal pyramidal coordination,[51,52] providing further evidence for the impact of the stereochemically active $4s^2$ lone pair of Ge^{2+}. The local structural distortion due to the displaced Ge^{2+} cations may be quantified through the evaluation of bond length (γ_x) and angle (γ_θ) distortion parameters for the GeS_4 tetrahedra (calculation details in ESI†). In the case of the near-ideal FeS_4 and $Ge^{4+}S_4$ tetrahedra located at the 4b site, γ_x (4.12×10^{-4}) and γ_θ (3.1×10^{-4}) for the (Fe, Ge)–S bonds are quite low, consistent with a near-tetrahedral coordination. However, for Ge–S bonds associated with the displaced Ge^{2+} cations, γ_x and γ_θ increase to 1.33×10^{-2} and 8.61×10^{-3}, respectively, indicating significant displacement of the Ge^{2+} cations from the centre of the GeS_4 tetrahedron.

The lattice thermal conductivity of Ge-substituted phases, κ_L, was modelled according to the Debye Callaway model:[53,54]

$$\kappa_L = \frac{k_B}{2\pi v_m}\left(\frac{k_B T}{\hbar}\right)^3 \int_0^{\theta_D/T} \frac{x^4 e^x}{\tau_c^{-1}(e^x-1)^2}\,dx \quad (1)$$

where $x = \hbar\omega/k_B T$, k_B = Boltzmann's constant, $\hbar$ = reduced Plank's constant, v_m = mean sound velocity, ω = phonon frequency, θ_D = Debye temperature and τ_c^{-1} = total phonon relaxation rate which can be expanded into:

$$\tau_c^{-1} = \tau_B^{-1} + \tau_D^{-1} + \tau_U^{-1} = \frac{v_m}{L} + A\omega^4 + B\omega^2 T\, e^{-\theta_D/3T} \quad (2)$$

where τ_B^{-1}, τ_D^{-1} and τ_U^{-1} represent the relaxation times due to grain boundary, point defect and phonon–phonon Umklapp scattering processes, respectively. L is the average grain size and A and B are fitting parameters, corresponding to the contributions of the point defect and Umklapp scattering processes, respectively. The point defect parameter (A) further depends on a scattering parameter, $\Gamma = \Gamma_M + \Gamma_S$, where Γ_M and Γ_S are the scattering parameters for mass-difference and strain-field fluctuations, respectively.[55,56] The calculation details for these parameters are given in the ESI† and the results presented in Table 2.

The point defect scattering parameter (A) increases significantly with Ge concentration, primarily due to a marked increase in the strain-field fluctuation (Γ_S). There is a 9-fold increase in Γ_S between compositions with $x = 0.02$ and $x = 0.06$, which suggests a high strain induced by the Ge substituent. This may reflect the local structural distortion associated with

Table 2 The fitted parameters from the Debye–Callaway model. ε is the impact of the stereochemically active adjustable parameter calculated from fitting eqn (1) to the experimental κ_L

Sample	L [μm]	A [$\times 10^{43}$ s^{-3}]	B [$\times 10^{43}$ s^{-3}]	Γ [$\times 10^{-3}$]	Γ_M [$\times 10^{-3}$]	Γ_S [$\times 10^{-3}$]	ε
$x = 0$	12.1	2	6	—	—	—	—
$x = 0.02$	5.9	7.26	6.2	8.11	0.66	7.45	88
$x = 0.06$	3.8	75.33	5.7	69.11	1.89	67.22	267
$x = 0.1$	19.6	97.47	6	85.99	3.02	82.97	200

the $4s^2$ lone pair of Ge^{2+}. The values of Γ_S determined in the present study are found to be higher than values reported for other substituted chalcopyrites containing non-lone-pair cations.[20,25,31] This suggests the presence of a cation with a stereochemically-active lone pair creates a high degree of strain, through a local structural distortion. The distortion enhances point defect scattering and lattice softening, as evidenced by the reduction in the elastic moduli, Debye temperature and sound velocities (Table 1).

Phonon calculations for the parent phase, $CuFeS_2$, (Fig. S7†) demonstrate that the majority of the heat-carrying acoustic modes lie below 4 THz while the low-frequency optical phonon modes are in the range 4–6 THz. In $CuFe_{0.94}Ge_{0.06}S_2$, the weak local chemical bonding of germanium with sulphur, leads to sharp resonant phonon states around 3–3.2 THz (Fig. 11). These localized vibrational modes are close in energy to both the acoustic and low-energy optical modes, and may contribute to enhanced phonon scattering. In addition, the lattice softening induced by Ge substitution propagates to the Cu–S and Fe–S bonds in the neighbouring MS_4 (M = Cu, Fe) tetrahedra, leading to changes in the detail of the phonon DOS compared to that of $CuFeS_2$.

Calculation of the phonon group velocities of the two longitudinal (LA, LA′) and one transverse optical (TO) acoustic modes (Table S5†) shows a reduction in the average group velocity along the $\Gamma - X$, $\Gamma - Z$ and $\Gamma - N$ directions in $CuFe_{0.94}Ge_{0.06}S_2$, compared to the pristine $CuFeS_2$, by *ca.* 2–6%. A similar combination of a local structural distortion and a reduction in the phonon group velocities has been observed for indium substitution in $CuFeS_2$.[29,30] The distortion has been attributed to a stereochemically-active $5s^2$ lone pair of electrons associated with In^+. Together with the results presented here, this suggests that the introduction of a p-block cation with a stereochemically-active lone pair of electrons, at one of the cation sites in $CuFeS_2$, offers an effective method for reducing the lattice thermal conductivity compared to what is achievable using transition-metal substituents.

The maximum figure-of-merit (zT) of $CuFe_{1-x}Ge_xS_2$ ($0.0 \leq x \leq 0.10$) increases from $zT = 0.07$ (at 723 K) for the pristine $CuFeS_2$ to a $zT = 0.4$ at 723 K for $CuFe_{0.94}Ge_{0.06}S_2$ (Fig. 12). This represents an almost six-fold improvement. Furthermore, the maximum value of zT attained in this work, is higher than the values reported for many of the substituted $CuFeS_2$ compositions,[20,25–27,29–31,57–59] and is one of the highest achieved in substituted chalcopyrite; thus, making Ge substitution a promising approach to fabricating high-performing n-type $CuFeS_2$ materials for thermoelectric applications.

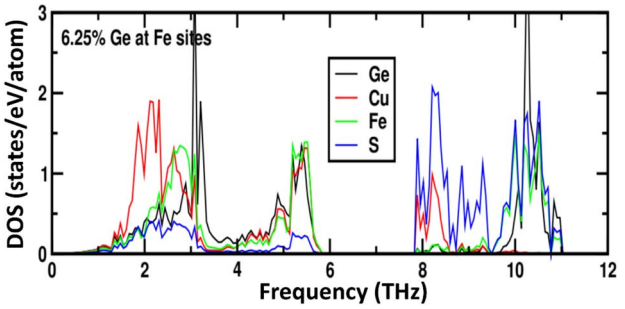

Fig. 11 The phonon density of states as a function of phonon frequency for 6.25 at% Ge-substituted $CuFeS_2$.

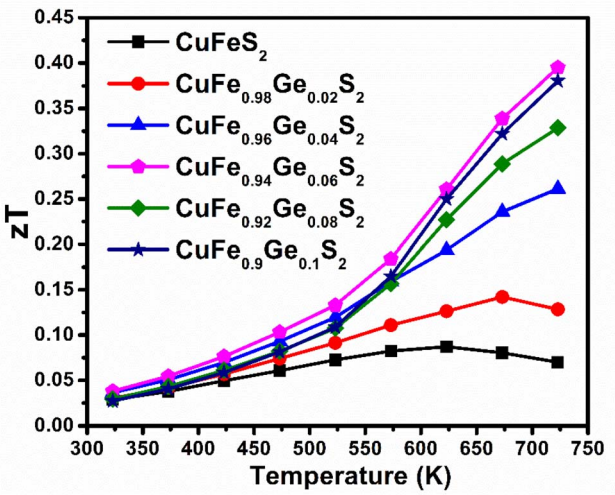

Fig. 12 Thermoelectric figure-of-merit as a function of temperature for $CuFe_{1-x}Ge_xS_2$ ($x = 0-0.1$).

4. Conclusions

Pair-distribution function analysis (PDF) reveals that substitution of iron in chalcopyrite by germanium leads to a local structural distortion associated with the presence of Ge^{2+} that is identified by XPS. The stereochemically-active $4s^2$ lone-pair of Ge^{2+} favours adoption of a trigonal pyramidal coordination which induces movement of the germanium cation from the centre of the tetrahedron towards one of the triangular faces. This contributes to the increase in the calculated strain-fluctuation scattering parameter (Γ_S), which leads to a reduction in lattice thermal conductivity. In addition, calculations indicate Ge substitution introduces localized vibrational modes, which may also increase phonon scattering through interaction with energetically similar acoustic and low-energy optic modes.

Substitution also produces a significant reduction in electrical resistivity as a result of an increased carrier concentration, although the increase is less than expected on the basis of electron counting. This can be attributed to the mixed Ge^{2+}/Ge^{4+} oxidation states indicated by XPS. However, the localized electronic states near the Fermi level arising from Ge, lead to a high density-of-states effective mass. This enables a relatively high Seebeck coefficient to be maintained, even at increased carrier concentrations, contributing to a high power factor of *ca.* 0.6 mW m^{-1} K^{-2} at 723 K in $CuFe_{0.94}Ge_{0.06}S_2$.

In conjunction with the marked reductions in thermal conductivity, the figure-of-merit of all Ge-substituted materials is increased over that of the end-member phase, with a maximum $zT = 0.4$ being attained for $CuFe_{0.94}Ge_{0.06}S_2$ at

723 K. These results demonstrate that substitution with a p-block cation, possessing a stereochemically-active lone pair of electrons can be an effective strategy to achieve high thermoelectric performance by effecting significant reductions in lattice thermal conductivity through local structural distortions.

Conflicts of interest

There are no conflicts to declare.

Acknowledgements

This work was funded by UKRI Global Challenges Research Fund (GCRF) supported by EPSRC, UK (grant no: EP/T020040/1). We would like to acknowledge the Diamond Light Source, UK for provision of beam time on I15-1 beamline under proposal CY30162. We acknowledge access to SuperSTEM, the National research facility for advanced electron microscopy, funded by EPSRC (EP/W021080/1). We also thank the Chemical Analysis Facility (CAF) at the University of Reading, Reading, UK.

References

1 L. D. Zhao, H. J. Wu, S. Q. Hao, C. I. Wu, X. Y. Zhou, K. Biswas, J. Q. He, T. P. Hogan, C. Uher, C. Wolverton, V. P. Dravid and M. G. Kanatzidis, *Energy Environ. Sci.*, 2013, **6**, 3346–3355.
2 Y. Wu, Z. Chen, P. Nan, F. Xiong, S. Lin, X. Zhang, Y. Chen, L. Chen, B. Ge and Y. Pei, *Joule*, 2019, **3**, 1276–1288.
3 C. Chang, M. Wu, D. He, Y. Pei, C. F. Wu, X. Wu, H. Yu, F. Zhu, K. Wang, Y. Chen, L. Huang, J. F. Li, J. He and L. D. Zhao, *Science*, 2018, **360**, 778–783.
4 B. Qin, D. Wang, W. He, Y. Zhang, H. Wu, S. J. Pennycook and L. D. Zhao, *J. Am. Chem. Soc.*, 2019, **141**, 1141–1149.
5 C. Zhang, M. de la Mata, Z. Li, F. J. Belarre, J. Arbiol, K. A. Khor, D. Poletti, B. Zhu, Q. Yan and Q. Xiong, *Nano Energy*, 2016, **30**, 630–638.
6 W. H. Shin, J. W. Roh, B. Ryu, H. J. Chang, H. S. Kim, S. Lee, W. S. Seo and K. Ahn, *ACS Appl. Mater. Interfaces*, 2018, **10**, 3689–3698.
7 A. V. Powell, *J. Appl. Phys.*, 2019, **126**, 100901.
8 R. Freer, D. Ekren, T. Ghosh, K. Biswas, P. Qiu, S. Wan, L. D. Chen, S. Han, C. Fu, T.-J. Zhu, A. K. M. A. Shawon, A. Zevalkink, K. Imasato, G. J. Snyder, M. Ozen, K. Saglik, U. Aydemir, R. Cardoso-Gil, E. Svanidze, R. Funahashi, A. V. Powell, S. Mukherjee, S. Tippireddy, P. Vaqueiro, F. Gascoin, T. Kyratsi, S. Philipp and T. Mori, *JPhys Energy*, 2022, **4**, 022002.
9 L. Paradis-Fortin, G. Guélou, V. Pavan Kumar, P. Lemoine, C. Prestipino, O. Merdrignac-Conanec, G. R. Durand, S. Cordier, O. I. Lebedev and E. Guilmeau, *J. Alloys Compd.*, 2020, **831**, 154767.
10 K. Suekuni, F. S. Kim, H. Nishiate, M. Ohta, H. I. Tanaka and T. Takabatake, *Appl. Phys. Lett.*, 2014, **105**, 132107.
11 C. Candolfi, G. Guélou, C. Bourgès, A. R. Supka, R. A. R. Al Orabi, M. Fornari, B. Malaman, G. Le Caër, P. Lemoine, V. Hardy, J.-M. Zanotti, R. Chetty, M. Ohta, K. Suekuni and E. Guilmeau, *Phys. Rev. Mater.*, 2020, **4**, 025404.
12 Y. Bouyrie, M. Ohta, K. Suekuni, Y. Kikuchi, P. Jood, A. Yamamoto and T. Takabatake, *J. Mater. Chem. C*, 2017, **5**, 4174–4184.
13 S. O. J. Long, A. V. Powell, P. Vaqueiro and S. Hull, *Chem. Mater.*, 2018, **30**, 456–464.
14 K. Chen, C. Di Paola, B. Du, R. Zhang, S. Laricchia, N. Bonini, C. Weber, I. Abrahams, H. Yan and M. Reece, *J. Mater. Chem. C*, 2018, **6**, 8546–8552.
15 X. Lu, D. T. Morelli, Y. Xia and V. Ozolins, *Chem. Mater.*, 2015, **27**, 408–413.
16 S. Tippireddy, R. Chetty, M. H. Naik, M. Jain, K. Chattopadhyay and R. C. Mallik, *J. Phys. Chem. C*, 2018, **122**, 8735–8749.
17 S. He, Y. Luo, L. Xu, Y. Wang, Z. Han, X. Li and J. Cui, *Inorg. Chem.*, 2021, **60**, 11120–11128.
18 J. Corps, P. Vaqueiro, A. Aziz, R. Grau-Crespo, W. Kockelmann, J. C. Jumas and A. V. Powell, *Chem. Mater.*, 2015, **27**, 3946–3956.
19 C. Bourgès, T. Barbier, G. Guélou, P. Vaqueiro, A. V. Powell, O. I. Lebedev, N. Barrier, Y. Kinemuchi and E. Guilmeau, *J. Eur. Ceram. Soc.*, 2016, **36**, 1183–1189.
20 B. Ge, J. Hu, Z. Shi, H. Wang, H. Xia and G. Qiao, *Nanoscale*, 2019, **11**, 17340–17349.
21 B. Du, R. Zhang, K. Chen, A. Mahajan and M. J. Reece, *J. Mater. Chem. A*, 2017, **5**, 3249–3259.
22 C. Bourgès, P. Lemoine, O. I. Lebedev, R. Daou, V. Hardy, B. Malaman and E. Guilmeau, *Acta Mater.*, 2015, **97**, 180–190.
23 S. Mukherjee, A. V. Powell, D. J. Voneshen and P. Vaqueiro, *J. Solid State Chem.*, 2022, **314**, 123425.
24 S. R. Hall and J. M. Stewart, *Acta Crystallogr., Sect. B: Struct. Crystallogr. Cryst. Chem.*, 1973, **29**, 579–585.
25 H. Xie, X. Su, G. Zheng, T. Zhu, K. Yin, Y. Yan, C. Uher, M. G. Kanatzidis and X. Tang, *Adv. Energy Mater.*, 2017, **7**, 1601299.
26 R. Lefèvre, D. Berthebaud, M. Y. Mychinko, O. I. Lebedev, T. Mori, F. Gascoin and A. Maignan, *RSC Adv.*, 2016, **6**, 55117–55124.
27 J. Navratil, J. Kašparová, T. Plecháček, L. Beneš, Z. Olmrová-Zmrhalová, V. Kucek and Č. Drašar, *J. Electron. Mater.*, 2019, **48**, 1795–1804.
28 B. Ge, Z. Shi, C. Zhou, J. Hu, G. Liu, H. Xia, J. Xu and G. Qiao, *J. Alloys Compd.*, 2019, **809**, 151717.
29 H. Xie, X. Su, S. Hao, C. Zhang, Z. Zhang, W. Liu, Y. Yan, C. Wolverton, X. Tang and M. G. Kanatzidis, *J. Am. Chem. Soc.*, 2019, **141**, 18900–18909.
30 B. Ge, H. Lee, C. Zhou, W. Lu, J. Hu, J. Yang, S.-P. Cho, G. Qiao, Z. Shi and I. Chung, *Nano Energy*, 2022, **94**, 106941.
31 S. Tippireddy, F. Azough, Vikram, F. T. Tompkins, A. Bhui, R. Freer, R. Grau-Crespo, K. Biswas, P. Vaqueiro and A. V. Powell, *Chem. Mater.*, 2022, **34**, 5860–5873.
32 J. Rodríguez-Carvajal, in *Abstracts of the Satellite Meeting on Powder Diffraction of the XV Congress of the IUCr*, Toulouse, France, 1990, p. 127.

33 A. K. Soper and E. R. Barney, *J. Appl. Crystallogr.*, 2011, **44**, 714–726.
34 C. L. Farrow, P. Juhas, J. W. Liu, D. Bryndin, E. S. Boin, J. Bloch, T. Proffen and S. J. L. Billinge, *J. Phys.: Condens. Matter*, 2007, **19**, 335219.
35 N. Fairley, V. Fernandez, M. Richard-Plouet, C. Guillot-Deudon, J. Walton, E. Smith, D. Flahaut, M. Greiner, M. Biesinger, S. Tougaard, D. Morgan and J. Baltrusaitis, *Appl. Surf. Sci. Adv.*, 2021, **5**, 100112.
36 G. Kresse and J. Furthmüller, *Comput. Mater. Sci.*, 1996, **6**, 15–50.
37 G. Kresse and J. Furthmüller, *Phys. Rev. B: Condens. Matter Mater. Phys.*, 1996, **54**, 11169–11186.
38 G. Kresse and J. Hafner, *Phys. Rev. B: Condens. Matter Mater. Phys.*, 1993, **47**, 558.
39 P. E. Blöchl, *Phys. Rev. B: Condens. Matter Mater. Phys.*, 1994, **50**, 17953.
40 J. P. Perdew, K. Burke and M. Ernzerhof, *Phys. Rev. Lett.*, 1996, **77**, 3865–3868.
41 S. L. Dudarev, G. A. Botton, S. Y. Savrasov, C. J. Humphreys and A. P. Sutton, *Phys. Rev. B: Condens. Matter Mater. Phys.*, 1998, **57**, 1505.
42 S. Grimme, J. Antony, S. Ehrlich and H. Krieg, *J. Chem. Phys.*, 2010, **132**, 154104.
43 P. E. Blöchl, O. Jepsen and O. K. Andersen, *Phys. Rev. B: Condens. Matter Mater. Phys.*, 1994, **49**, 16223.
44 X. Gonze, *Phys. Rev. A: At., Mol., Opt. Phys.*, 1995, **52**, 1086–1095.
45 X. Gonze, *Phys. Rev. A: At., Mol., Opt. Phys.*, 1995, **52**, 1096–1114.
46 A. Togo and I. Tanaka, *Scr. Mater.*, 2015, **108**, 1–5.
47 R. D. Shannon, *Acta Crystallogr., Sect. A: Cryst. Phys., Diffr., Theor. Gen. Crystallogr.*, 1976, **32**, 751–767.
48 I. Nakai, Y. Sugitani, K. Nagashima and Y. Niwa, *J. Inorg. Nucl. Chem.*, 1978, **40**, 789–791.
49 A. Ghahremaninezhad, D. G. Dixon and E. Asselin, *Electrochim. Acta*, 2013, **87**, 97–112.
50 G. Eulenberger, *J. Less-Common Met.*, 1985, **108**, 65–72.
51 W. H. Zachariasen, *Phys. Rev.*, 1932, **40**, 917–922.
52 V. G. Bissert and K.-F. Hesse, *Acta Crystallogr., Sect. B: Struct. Crystallogr. Cryst. Chem.*, 1978, **34**, 1322–1323.
53 J. Callaway, *Phys. Rev.*, 1959, **113**, 1046–1051.
54 J. Callaway and H. C. von Bayer, *Phys. Rev.*, 1960, **120**, 1149–1154.
55 G. A. Slack, *Phys. Rev.*, 1957, **105**, 829.
56 B. Abeles, *Phys. Rev.*, 1963, **131**, 1906–1911.
57 H. Xie, X. Su, G. Zheng, Y. Yan, W. Liu, H. Tang, M. G. Kanatzidis, C. Uher and X. Tang, *J. Phys. Chem. C*, 2016, **120**, 27895–27902.
58 W. D. Carr and D. T. Morelli, *J. Electron. Mater.*, 2016, **45**, 1346–1350.
59 J. Li, Q. Tan and J. F. Li, *J. Alloys Compd.*, 2013, **551**, 143–149.